

RESEARCH ARTICLE **Vulcan: A deep-towed CSEM receiver**

10.1002/2015GC006174

Key Points:

- A deep-towed, fixed-offset, marine EM receiver can be used to image seafloor resistivity
- A rigid body reduces noise and allows vertical electric fields to be measured
- Applications include mapping seafloor gas hydrate and other shallow geology

Correspondence to:S. Constable,
sconstable@ucsd.edu**Citation:**Constable, S., P. K. Kannberg, and K. Weitemeyer (2016), Vulcan: A deep-towed CSEM receiver, *Geochem. Geophys. Geosyst.*, 17, doi:10.1002/2015GC006174.

Received 10 NOV 2015

Accepted 18 FEB 2016

Accepted article online 22 FEB 2016

Steven Constable¹, Peter K. Kannberg¹, and Karen Weitemeyer²¹Scripps Institution of Oceanography, University of California San Diego, La Jolla, California, USA, ²Advisian, WorleyParsons Group, Calgary, Alberta, Canada

Abstract We have developed a three-axis electric field receiver designed to be towed behind a marine electromagnetic transmitter for the purpose of mapping the electrical resistivity in the upper 1000 m of seafloor geology. By careful adjustment of buoyancy and the use of real-time monitoring of depth and altitude, we are able to deep-tow multiple receivers on arrays up to 1200 m long within 50 m of the seafloor, thereby obtaining good coupling to geology. The rigid body of the receiver is designed to reduce noise associated with lateral motion of flexible antennas during towing, and allows the measurement of the vertical electric field component, which modeling shows to be particularly sensitive to near-seafloor resistivity variations. The positions and orientations of the receivers are continuously measured, and realistic estimates of positioning errors can be used to build an error model for the data. During a test in the San Diego Trough, offshore California, inversions of the data were able to fit amplitude and phase of horizontal electric fields at three frequencies on three receivers to about 1% in amplitude and 1° in phase and vertical fields to about 5% in amplitude and 5° in phase. The geological target of the tests was a known cold seep and methane vent in 1000 m water depth, which inversions show to be associated with a 1 km wide resistor at a depth between 50 and 150 m below seafloor. Given the high resistivity (30 Ωm) and position within the gas hydrate stability field, we interpret this to be massive methane hydrate.

1. Introduction

The marine controlled-source electromagnetic (CSEM) sounding method was developed in the early 1980s in order to study the geology of the oceanic lithosphere [Cox, 1981; Sinha *et al.*, 1990]. In these early studies, several (of order 10) ocean-bottom electric field (OBE) receivers were deployed with an electric dipole transmitter towed on or close to the seafloor broadcasting at frequencies around 1 Hz. A typical OBE receiver has two orthogonal electric field antennas 8–10 m long, but because OBE noise at CSEM frequencies is dominated by the amplifiers, equipping instruments with longer (100–3000 m) single antennas [Webb *et al.*, 1985] creates a bigger signal and allows maximum source-receiver ranges of 20–100 km to be achieved. At these offsets, one can image the entire crust and the uppermost mantle [e.g., Constable and Cox, 1996; MacGregor *et al.*, 2001; Key *et al.*, 2012].

In the early 2000s, the CSEM method was adopted for offshore hydrocarbon exploration [Ellingsrud *et al.*, 2002; Constable, 2010]. Industry operations usually include magnetic field sensors (ocean-bottom electromagnetic, OBEM, receivers, or “nodes” in industry parlance) and the number of receivers is increased to of order 100. Since hydrocarbon targets are often buried several kilometers below the seafloor, source-receiver offsets are still maximized because of the thick sequences of highly conducting sediments on the continental shelves. Even with very large transmitter currents (over 1000 A), maximum ranges are only about 10 km for instruments with 10 m antennas because of attenuation in conductive sediments. Typical OBEM spacing for hydrocarbon exploration is 2–5 km.

In addition to the deep tectonic and hydrocarbon targets, there are geologically interesting targets in the shallower parts of the seafloor section, such as gas hydrates, submarine massive sulfides (SMS), hydrothermal systems, and offshore groundwater. By decreasing seafloor receiver spacing to about 600 m to improve resolution in the shallow section, the OBEM-based CSEM method has been successfully used to study gas hydrate in the shallow seafloor [Weitemeyer *et al.*, 2006; Weitemeyer and Constable, 2010; Weitemeyer *et al.*, 2010]. However, there are a number of limitations to the deployed receiver approach. Closely-spaced arrays of seafloor receivers are costly in terms of instrumentation and ship time for deployments and recoveries.

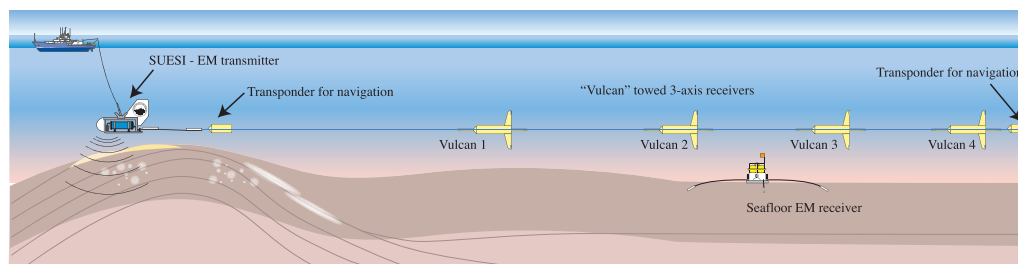


Figure 1. Typical array of four Vulcan instruments along with transponder navigation packages at the end of the transmitter antenna and the receiver array. Total lengths of between 500 and 1200 m have been used to date. The towed array is often used in conjunction with deployed OBEM instruments.

Navigational errors in transmitter position contribute to large errors in CSEM data at short source-receiver offsets [e.g., Myer *et al.*, 2012]. High gain seafloor receivers can saturate at short offsets. Finally, even with closely spaced instruments, there are inevitably gaps in data coverage between receivers.

For near-seafloor surveys in shallow water, commercially available land EM systems can be adapted for marine use [e.g., Müller *et al.*, 2011, 2012; Goldman *et al.*, 2011], but in deep water (where, for example, gas hydrate is found), customized equipment must be developed. Deep-water bottom-towed electric and magnetic field systems have been developed and used effectively [Cheesman *et al.*, 1993; Yuan and Edwards, 2000; Evans, 2007; Schwalenberg *et al.*, 2010a; Schwalenberg and Engels, 2011]. However, bottom-towed systems have high noise levels (in some cases requiring the towing vessel to stop during measurements), and are exposed to the risk of getting damaged or detached by seafloor obstacles. As an alternative to bottom-towed systems, Goto *et al.* [2008] developed a DC electric field system with a 160 m array towed about 5 m above the seafloor behind an existing deep-towed camera system.

The limitations of OBEM-based surveys motivated us to develop towed receivers as a way to either supplement data from sparse arrays of seafloor receivers or as a stand-alone system for mapping shallow geology (Figure 1). Because our EM transmitter [Constable, 2013] is deep-towed 50–100 m above the seafloor, we developed a neutrally buoyant midwater system rather than a bottom-towed system. Our design is novel in that we use a rigid assembly rather than cabled arrays, a consequence of early measurements showing that towed cables suffer from noise associated with lateral motion of antennas in Earth's magnetic field. Also, synthetic modeling studies demonstrated the value of collecting vertical electric field data, and so our rigid body includes a vertical electric dipole receiver on a tail fin and, for completeness, a horizontal dipole on horizontal wings. Our instrument became nick-named "Vulcan" because the horizontal wing assembly of the first version resembled that of the Vulcan delta wing aircraft.

2. Existing Transmitter and Receiver Systems

The Scripps transmitter and receiver systems have been recently well documented by Constable [2013], but since they are an integral part of the Vulcan system the relevant features will be summarized here.

Our EM transmitter, SUESI (Scripps Undersea Electromagnetic Source Instrument), consists of a surface power supply/control system and a deep-towed package that contains the power rectification and switching electronics, microprocessor controller, communication systems, and assorted navigation sensors. The surface and deep-towed systems are connected by a standard 17 mm coaxial armored oceanographic cable. The surface system generates 400 Hz power for transmission down the tow cable at 600–2000 VAC, the phase of which is controlled by a GPS clock—in this way accurate time is carried down to the deep-tow package on the power supply. In the deep-tow package, the 2000 VAC power is transformed down to about 40 VAC, rectified, and switched using insulated gate bipolar transistors (IGBTs) under computer control, to provide arbitrary binary or ternary waveforms switched in increments of 1/400 s time units. Maximum output current is 500 A (rarely used; 300–400 A is more typical). We use aluminum conductor antennas made neutrally buoyant with plastic jackets, typically 50–300 m long with a 10 m lead-in to the near electrode. Electrodes are 1–2 cm diameter soft copper tubing attached to the antennas using pipe fittings. We

typically use electrodes that are about 10% of the antenna length to minimize resistance to seawater while maintaining a dipole geometry.

A bidirectional, 9600 baud frequency-shift-keyed (FSK) communication system is overlain on the power supply using high voltage crossover networks. Downlink commands control the waveform geometry and frequency, synchronize GPS time to a minute mark, switch peripheral navigation systems on and off, stop and start transmission, and initiate a high-frequency snapshot of the waveform current. Uplink information includes samples every 3 s of voltage, current, and various temperatures measured throughout the switch-frame. When a current waveform snapshot is requested, the current is sampled at around 1 kHz, the data are buffered, and then transmitted to the vessel.

In the deep-tow package, there are four 4-conductor ports on underwater connectors to provide bidirectional RS-232 communication and switchable 24 VDC power to the outside world. These ports are connected to a Kongsberg acoustic altimeter, a Valeport conductivity-temperature-depth-sound velocity (CTDV) sensor, a Benthos DS-7000 long base line acoustic ranging system, and the Vulcan telemetry described below. In addition to these four ports, there are two switchable 24 VDC supplies for mission-specific instruments, an RS-232 version of the FSK communication for optional use with a fiber-optic deep-tow cable, and an output of the hall-effect current sensor used to measure output current and waveform.

The Scripps OBEM system is in the third significant iteration after starting life as a 16 bit OBE instrument using voltage-controlled oscillators for digitization (the "Mk-I" instrument, described by *Webb et al.* [1985] and *Constable and Cox* [1996]), which was replaced by an OBEM instrument using 16 bit multiplexing analog to digital conversion (ADC) (the "Mk-II" instrument, described by *Constable et al.* [1998]). The current "Mk-III" OBEM instrument uses eight channels of 24 bit ADC, records to a compact flash card, and has a low-power temperature compensated clock [*Constable*, 2013]. The amplifier and logging electronics are housed in a 14.5 cm diameter by 63 cm long pressure case rated to 6000 m water depth, and consume a total of about 400 mW power from rechargeable batteries.

3. Towed Receiver Development

The design of our towed electric field receiver was driven both by synthetic model studies and experiments with towed cable arrays, described in this section.

3.1. Cables Versus Rigid Antennas

We started experimenting with towed receiver instruments in mid-2004, during the Hydrate Ridge experiment described in *Weitemeyer et al.* [2006]. A standard Mk III seafloor electric field logger was trimmed neutrally buoyant with syntactic foam and attached to an array of electrodes on a multiconductor cable. The array was 170 m long, divided into a series assembly of two 10 m and two 75 m antennas. The logger and electrodes were towed 500 m behind the SUESI and the entire system was towed about 100 m above the seafloor as part of an OBEM based CSEM survey. Unfortunately a technical fault prevented data collection, but we carried out noise tests using this array in 2006, deploying it at a depth of 100 m and varying the tow speed. We observed that noise was generally lower at higher tow speeds. This suggested that the main source of noise is associated with the cable moving laterally or vertically with velocity \mathbf{v} in Earth's magnetic field \mathbf{B} , inducing a Lorentz-type electric field $\mathbf{E} = \mathbf{v} \times \mathbf{B}$. At higher speeds and tensions, we infer that lateral movement is reduced. Further, this observation also suggested that streaming potentials, thought to be a problem with towed electrodes [*Evans*, 2007], are not a problem with our type of silver-silver chloride electrode (described in *Webb et al.* [1985] and *Constable* [2013]), since one would expect streaming potentials to be proportional to velocity.

3.2. Sensitivity in the Vertical Electric Field

Motivation for developing a towed receiver instrument came largely from our interest in mapping submarine gas hydrate, which can vary laterally in its distribution and may be associated with methane migration along steeply dipping faults [e.g., *Cook et al.*, 2008; *Riedel et al.*, 2010]. All previously developed towed receiver systems use an inline source and receiver, since this geometry is much easier to drag across the seafloor or tow through seawater. However, our numerical modeling of possible hydrate targets suggested that in some circumstances the vertical electric field may carry more information than the inline electric field for laterally heterogeneous structure. This is illustrated in Figure 2. We modeled a hydrate-filled, steeply

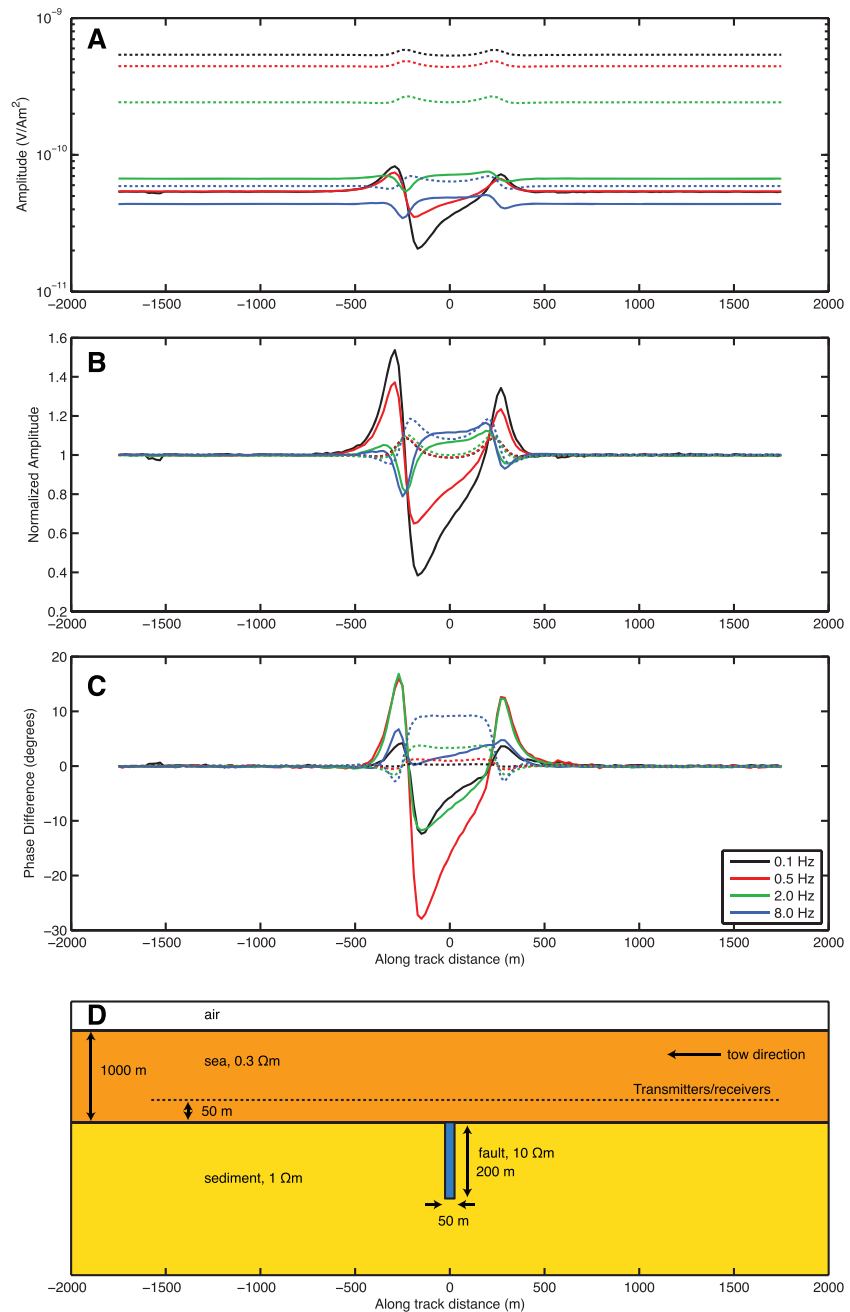


Figure 2. A simple 2-D model of a 10 Ωm hydrate-filled fault, 50 m wide and 200 m tall, buried in a 1 Ωm half-space (d). Water depth is 1000 m, not to scale. The model response is computed for a 500 m source-receiver offset towed 50 m above the seafloor, at four frequencies between 0.1 and 8 Hz. Horizontal (broken lines) and vertical (solid lines) electric fields are modeled for a horizontal electric dipole transmitter, plotted at the midpoint of the transmitter and receiver, with the transmitter to the left (i.e., being towed from right to left). (a) Field amplitudes; (b) and (c) show normalized amplitudes and phase differences.

dipping fault using the 2-D finite element code of *Key and Ovall* [2011], assuming point dipoles for source and receiver. The figure shows the inline (E_y) and vertical (E_z) electric fields modeled 500 m behind a horizontal electric field transmitter which is towed 50 m above the model seafloor. Note that the horizontal width of the model response is determined by the source-receiver spacing, not the width of the target structure.

The E_z amplitude response away from the target is largely independent of frequency, and over the target E_z amplitude is largest at the lowest frequency while the E_z phase response is largest at the higher

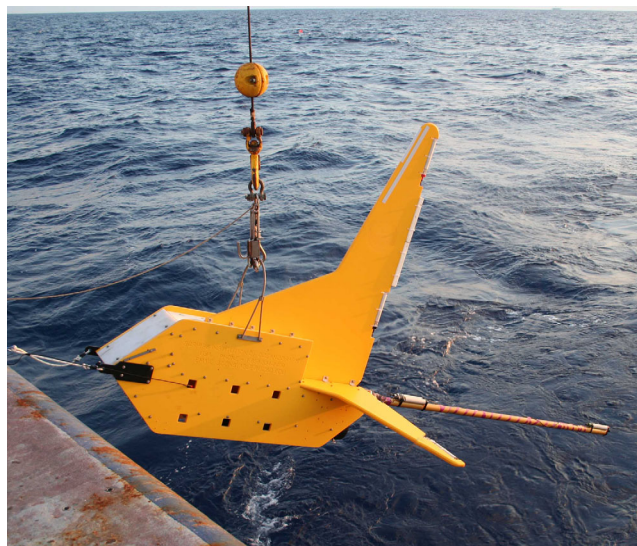


Figure 3. Photograph of the Mk-I Vulcan instrument being deployed.

Hz is the E_y response slightly larger than the E_z response, at which point the amplitude of the E_y response is as small as that of E_z .

There generally appears to be more information in the vertical electric field data. Although the amplitude of the E_y response increases with frequency, the shape of the response is similar across the spectrum. However, the shape of the E_z response changes with frequency, particularly for amplitude, which reverses sign. Because of reciprocity, as an E_y transmitter and E_y receiver are towed across a conductivity contrast, the response must be symmetrical and the same going from high resistivity to low resistivity and vice versa. However, for an E_y transmitter and E_z receiver, the direction of the resistivity contrast makes a difference, resulting in a distinct asymmetry to the E_z response.

3.3. Vulcan Mk-I Instrument

A logistical inconvenience of cable-based antenna systems is that a pressure case containing the data logger, amplifiers, and batteries needs to be made neutrally buoyant and attached to the cable close to the electrode antennas (given the small signal levels and the noise from cable motion, one does not want to transmit un-amplified signals any great distance). For a tow body with rigid antennas, the logger can be incorporated into the frame holding the antennas. The design approach of our first Vulcan system was to build an instrument around a standard Mk III seafloor data logger [Constable, 2013] made positively buoyant using three 10" (25.4 cm) diameter oceanographic glass spheres. This assembly was housed in a box constructed of polyethylene sheet (slightly buoyant itself) to which a vertical tail was attached for a 1 m vertical electric dipole and a pair of horizontal wings for a 2 m cross-line dipole. The 2 m inline dipole was mounted on a very rigid tube made from spun para-aramid fiber that projected from the rear of the device. Our standard 25 cm silver-silver chloride electrode [Constable, 2013] was used for all three dipoles. Lead weights were used in the base of the frame to trim the system to a slight positive buoyancy and make it float horizontally. The final assembly is shown in Figure 3.

The Mk-I Vulcan was towed behind our EM transmitter (SUESI) using a fixed length of neutrally buoyant rope. In order to obtain the orientation of the instrument, we attached a Honeywell HMR3400 compass module in an external pressure case. This device puts out a serial data stream of heading and attitude (pitch and roll), but no timing information. We also attached a Digiquartz Paroscientific pressure sensor for depth information, which again outputs serial data with no timing. In order to use these data streams, we developed a serial data logger that has a real-time clock to time-stamp the incoming data streams from the depth and compass sensors and store them in flash memory. Time is set on the serial data logger before deployment and data recorded every few seconds during operation. The serial data logger and necessary batteries were housed in another pressure case mounted within the tow body.

frequencies. This suggests a mostly galvanic response to seafloor conductivity for the E_z component. However, the phase response at 0.1 Hz is still larger than any of the E_y phase responses. Although the amplitude of E_z at the lower frequencies is nearly an order of magnitude lower than that of E_y , there is a factor of two to three variation in response to the model structure, while there is barely a 20% response in the E_y amplitudes. As the frequency increases and inductive effects begin to contribute more to the signal, we see a significant target response in E_y phase as well as amplitude, but at 0.5 and 2.0 Hz the vertical field response is as large as, or larger than, the horizontal field response in both amplitude and phase. Only at 8

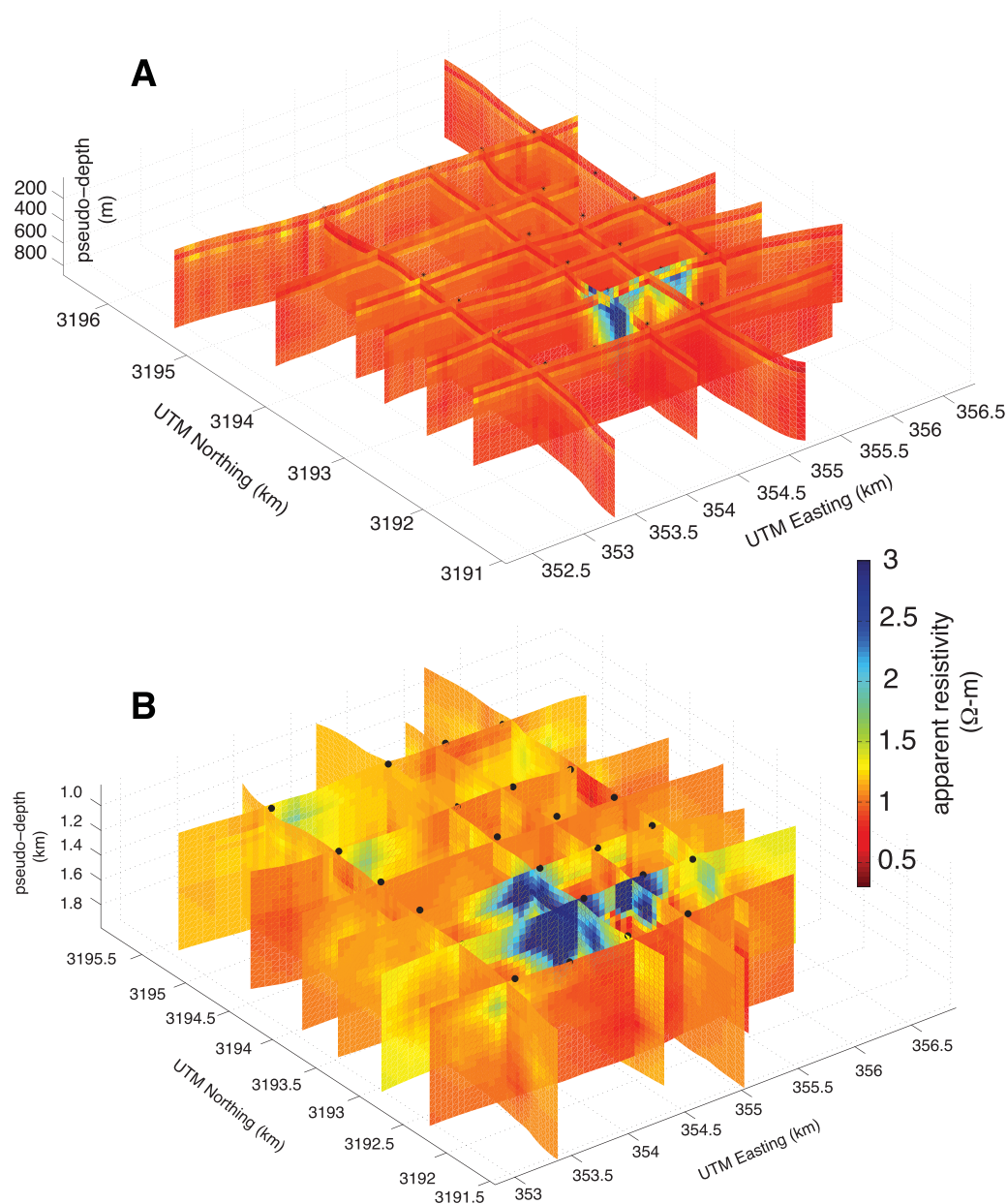


Figure 4. (a) Apparent resistivity pseudosections of Vulcan Mk-I data collected over block MC 118 in the Gulf of Mexico. The vertical scale is constructed by taking one skin depth at the lowest frequency processed. (b) Apparent resistivity pseudosections from ODEM data during the same survey, at a fixed frequency of 6.5 Hz using source-receiver offset projected at 45° for the vertical scale. From *Weitemeyer and Constable* [2010].

The Mk-I Vulcan was tested in early 2007 offshore San Diego and then used for a gas hydrate mapping project in the Gulf of Mexico in late 2008, which is described in *Weitemeyer and Constable* [2010]. Vulcan was flown 300 m behind SUESI during OBEM type CSEM surveys of four prospects on blocks AC 818, WR 313, GC 955, and MC 118. Since we had no acoustic navigation system on the Vulcan and no real-time depth information, we were initially cautious about flying close the seafloor, and kept the altitude to 100 m or higher on the first surveys, which limited the sensitivity of the Vulcan data. However, by the time we carried out the final survey on MC 118, we had enough experience to fly the system at 65 m altitude and obtained good sensitivity to seafloor resistivity.

CSEM surveys are sensitive to the depth of conductivity structure both geometrically, through source-receiver spacing, and parametrically, through the skin depths associated with different frequencies of

operation. For the Gulf of Mexico surveys, we had a single Vulcan at fixed offset, and so we had no variation in the sounding geometry. However, by transmitting the broad spectrum Waveform D of Myer *et al.* [2011], we have nearly two decades of frequency data available. For the Gulf of Mexico surveys, we processed seven frequencies between the fundamental (0.5 Hz) and the 67th harmonic (33.5 Hz), corresponding to skin depths in 1 Ω m sediment of 700 m to 86 m.

Figure 4 shows apparent resistivity pseudosections for Vulcan data collected over block MC 118 in the Gulf of Mexico, where we had 10 SUESI tow lines over 24 OBEM receivers. Instead of using the usual source-receiver offset, the pseudo-depth scale is generated by the skin depth distance in 1 Ω m material at each frequency and by fitting a half-space to the amplitude of the total electric field vector calculated from all three components. The depth should not be taken literally—pseudosections are notoriously unreliable and we are still subject to the geometrical constraints of our source-receiver offset—but it serves as a useful plotting parameter. The background resistivity is remarkably uniform at around 1 Ω m, and the cross-line ties are excellent. There is a slight artifact at the highest frequency processed, but this frequency is one of the most affected by uncertainties in transmitter and receiver navigation, transmitter waveform characterization, and receiver calibration. In the south-east quadrant of the survey higher resistivities associated with known methane, vents and outcropping gas hydrate are evident. Comparison with data from the deployed OBEM instruments, also shown in Figure 4, comes from fitting a half-space to the horizontal polarization ellipse maxima, and shows that the Vulcan system is collecting data comparable to the seafloor instruments at less effort and with less noise from navigation uncertainties.

The Gulf of Mexico results were encouraging, and the Vulcan-I system was used on the 2010 SERPENT project [Key *et al.* 2012] at a 500 m offset, and two Vulcans used at 250 m and 500 m offsets on the 2009 Scarborough project [Myer *et al.* 2012]. However, these projects highlighted the limitations of the Mk-I system. The package was cumbersome, being 4 m long and weighing about 100 kg, and needed to be deployed and recovered using a small crane or a line through a block on the vessel's A-frame pulled by a winch or capstan. Deploying two in tandem required complicated transfer of loads while the second instrument was deployed. Having no real-time depth or altitude information limited the source-receiver offsets that could be safely used without danger of hitting the seafloor. These factors drove the development of the Mk-II system.

4. Vulcan Mk-II Instrument System

Motivations for the design of the Mk-II system included the desire for multiple instruments to be easily installed on the towing line, and to increase the source-receiver offsets to around 1000 m. This required reducing the size of the instrument package, and replacing the artificial fiber towing line with an electromechanical cable that would allow depth information to be telemetered back to the SUESI and hence to the ship. The maximum depth capability of the Mk-I instrument was 6000 m. The Scripps Mk-II instruments were reduced to a 4000 m capability to save a little weight, although the Southampton Mk-II Vulcan [Goswami *et al.*, 2015] was built to maintain a 6000 m capability.

4.1. A Smaller Instrument Package

The Vulcan Mk-I prototype instrument was assembled with available components, such as the seafloor data logger, glass flotation, Paroscientific depth gauges packaged in commercial pressure cases, etc. In order to shrink the package in size for the Mk-II instrument, these functions were all consolidated into one pressure housing which was reduced in diameter from 5.75" (14.6 cm) to 5" (12.5 cm) and made more buoyant by making one end hemispherical (instead of a flat plate or end-cap). A Paroscientific sensor was purchased without the commercial pressure case and installed inside the logger case with an oil-filled capillary tube penetrating the logger end-cap. Similarly, the compass/pitch/roll sensor and the serial data logger were also included in the main pressure housing.

We created a new layout for the three-channel electric field amplifier circuit board to fit into the smaller pressure case, incorporating surface mount components wherever possible. We added a ST Microelectronics LIS344AI 3-axis accelerometer to the amplifier board in order to provide additional navigation data and possibly reference data for noise reduction in the electric field channels.

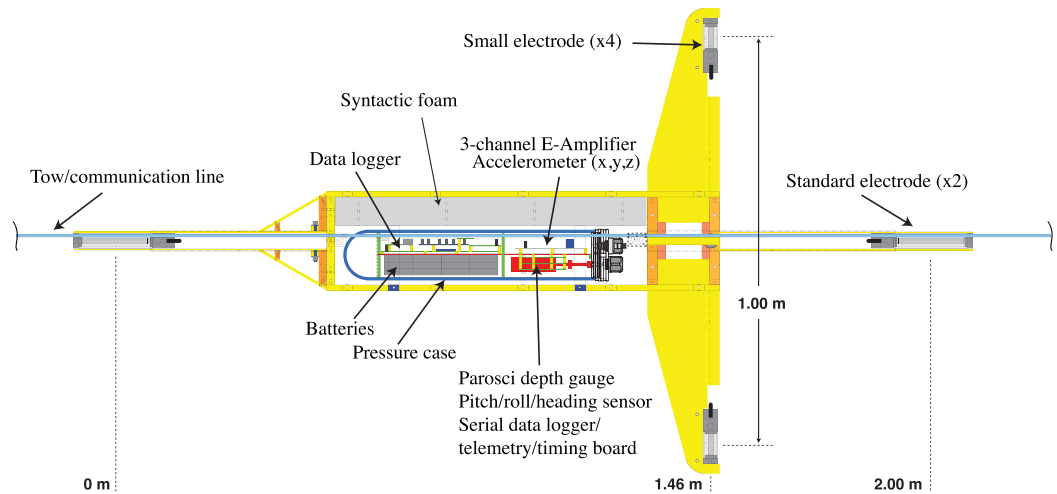


Figure 5. Cut-away schematic of the Mk-II Vulcan tow package.

Buoyancy is provided by a slab of syntactic foam situated above the pressure case (to provide a righting moment, which is also helped by mounting the batteries in the lower half of the pressure case). The tow body is again made out of polyethylene sheet, but is now a lot smaller and lighter. The 2 m horizontal inline electric dipole is maintained by positioning the forward electrode in front of the instrument housing, and the 1 m vertical dipole is maintained by including a second vertical fin on the bottom of the package. The horizontal wings now span only 1 m, but this component is least important, since with an ideal towing geometry the crossline electric field will be close to zero, and if this component is being used to create a polarization ellipse or to rotate the fields into the vertical direction there is no value in having it larger than the vertical dipole. To help achieve the vertical and crossline dipole lengths in a smaller package, electrodes were made that are half the length of our standard electrodes. The standard electrodes are still used on the inline dipole, since in theory these should be lower impedance and slightly lower noise. Figure 5 shows a drawing of the final assembly.

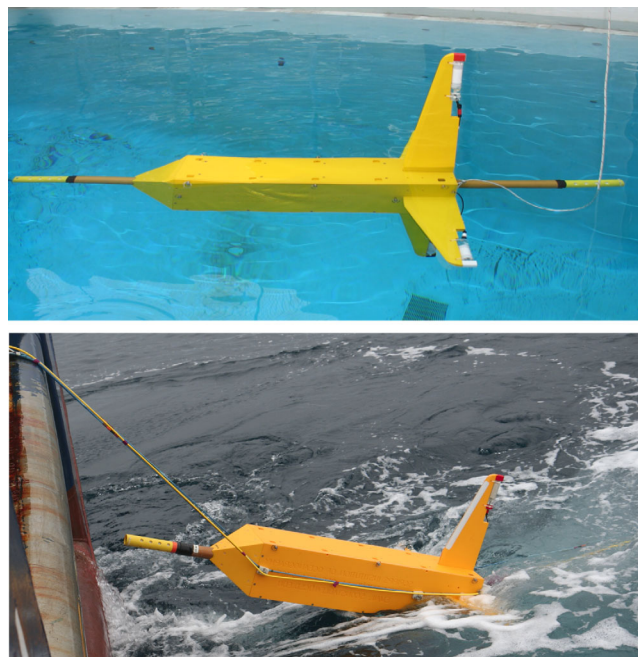


Figure 6. (top) Float testing the Vulcan Mk-II instrument. (bottom) Deployment of the instrument, showing the communication cable (yellow) and the split-line attachment system (blue).

As described below, the rope tow line is replaced with an electrical cable for telemetry, but at the positions where the Vulcan packages are attached we take the load with a split line of rope that allows the Vulcan tow body to be clipped into the array without transferring loads. A table bolted to the ship's deck with a slot for the bottom fin makes this a quick, easy, and safe operation. The only other action to install a Vulcan on the array is to connect the inboard and outboard electrical cables to each other and to Vulcan using a "Y" molded harness with underwater connectors. Figure 6 shows photographs of the assembly, which weighs 43 kg in air, Figure 7 shows a block diagram of the instrument package, and Table 1 summarizes the difference between the Vulcan systems and the OBEM instrument.

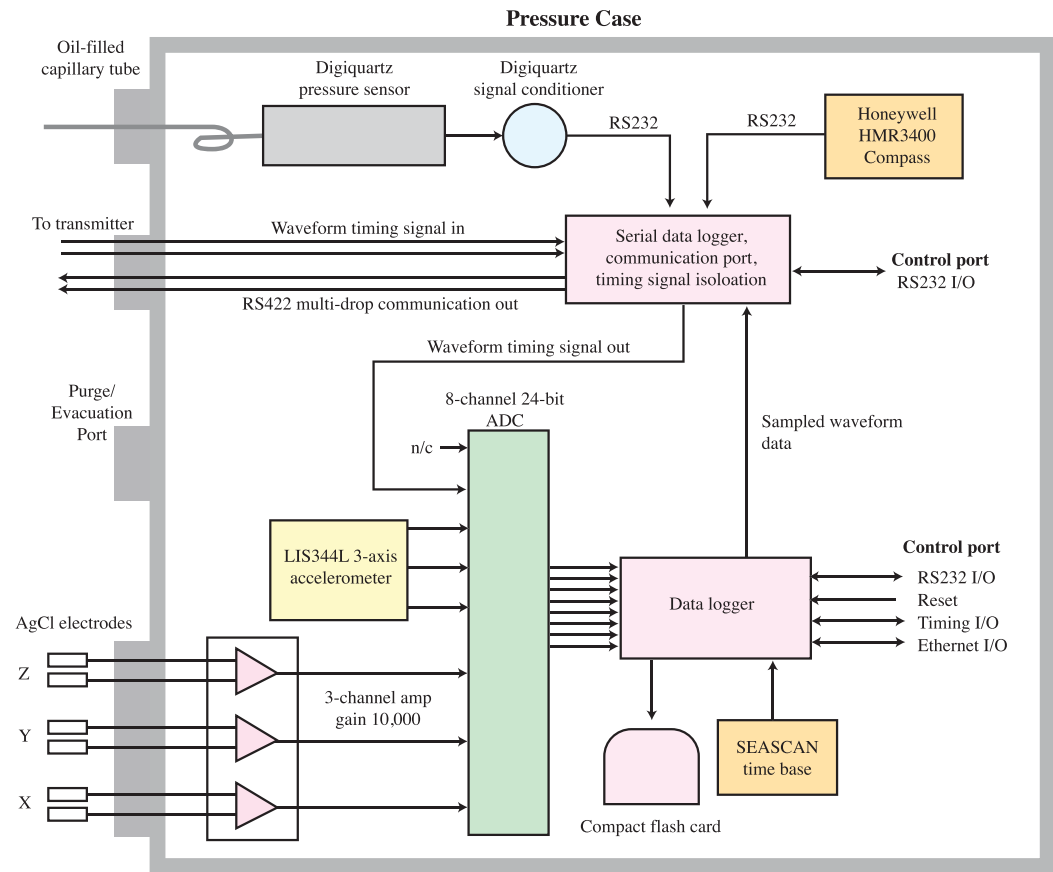


Figure 7. Block diagram of the Mk-II Vulcan instrument package.

Figure 1 shows a typical array using four Vulcan systems. In addition to the electric field receivers, we have a package at the end of the transmitter antenna which houses an acoustic navigation transponder, a Paroscientific depth gauge, compass/attitude sensor, and serial data logger (antenna tail-end transponder, or A-TET). A similar package is attached to the far end of the array, but with the addition of an acoustic altimeter which records the height of the tail end above the seafloor (called B-TET).

The actual spacings for the array involve some trade-offs. Transmitter antenna impedance is mainly determined by electrode length (longer electrodes have lower impedance), which we limit to about 10% of total length [Constable, 2013], so increasing antenna length increases dipole moment both from larger currents as well as the length. However, to approximate a dipole, we want the transmitter antenna to be a fraction of the range to the first Vulcan. Increasing total array length increases depth of sensitivity, at the cost of greater time to recover from turns and greater risk when towing over varying bathymetry. Short source-receiver offsets should increase resolution, but in practice navigation errors make interpreting short offset data difficult, and also increases error in the point dipole approximation for the transmitter.

Table 1. Comparison of Vulcan and OBEM Instruments

Instrument	Weight ^a	Ey Dipole ^b	Ex Dipole	Ez Dipole	Noise 1 Hz	Noise 10 Hz
OBEM	160 kg ^c	10 m	10 m	2 m	10 ⁻⁹ V/m/√Hz	10 ⁻⁹ V/m/√Hz
Vulcan Mk I	100 kg	2 m	2 m	1 m	10 ⁻⁷ V/m/√Hz	10 ⁻⁸ V/m/√Hz
Vulcan Mk II	43 kg	2 m	1 m	1 m	10 ⁻⁸ V/m/√Hz	10 ⁻⁹ V/m/√Hz

^aWeight is in air.
^bEy is inline, Ex is crossline.
^cNot including a 170 kg seafloor anchor.

In projects where we wish to maximize depth of resolution, we have used a 120 m transmitter antenna (10 m to the near electrode, 110 m to the far electrode, and 10 m of copper pipe for the electrodes) followed by a 400 m lead-in to the first Vulcan, 200 m between Vulcans after that, with a final 10 m for the B-TET, or 1130 m total [e.g., *Constable et al.*, 2012]. For operations where the survey includes a lot of turns, we have shortened the array to about 500 m total using a 50 m transmitter antenna to make the recovery from the turns faster.

4.2. Telemetry Between Vulcans and SUESI

In order to extend the array lengths, real-time information about the array depths is needed in order to avoid running afoul of the seafloor. Ultra-short baseline (USBL) acoustic systems are normally used for navigation of remotely operated vehicles, but with laybacks of over a kilometer USBL acoustics are not reliable, and are limited to total water depths of about 3 km at best. Academic studies are often carried out at full ocean depths of 4 km or more. We solve this problem by telemetering the output of the depth sensors in the Vulcans to the transmitter, which in turn telemeters the data to the research vessel.

To keep the tow cable light, simple, and inexpensive we did not want to dedicate communication wires to every device on the array, and standard RS-232 serial communication will not work over the 1000+ m ranges we tow the Vulcans. Instead we developed a RS-422 type multidrop telemetry that communicates by address on a single twisted pair of copper wires. The system has error and data collision detection and correction in case two or more devices try to communicate at the same time. At SUESI, a circuit in a small external pressure case converts the RS-422 protocol into RS-232 signals for communication over one of SUESI's auxiliary power/data ports. The microprocessor inside SUESI then includes the Vulcan data in the navigation/health data stream being sent to the research vessel. The multidrop telemetry has been tested on 4000 m cables.

Of course, this would be a potential application for fiber optic communication (FOC), but, while light, FOC is neither simple nor inexpensive, especially when used at great water depths. Furthermore, FOC systems are power hungry, and we have the dual problems of powering everything by batteries and avoiding noise in the nanovolt circuitry of the electric field sensors.

Our tow cable consists of two twisted pairs of polypropylene insulated 22 AWG copper wire, a para-aramid strength member, and an outer jacket of polyurethane. Outside diameter is 6.86 mm and the weight in water is 1.34 kg/100 m, necessitating the addition of some syntactic foam to achieve neutral buoyancy. The second twisted pair was originally used to send commands to adjustable wings, which we hoped to use to adjust the flying depth, but we discovered that at the slow tow speeds of marine CSEM there was not enough lift or depression force to move a kilometer length of cable having a cross-sectional area of 7 m². Instead, we rely on careful buoyancy trimming, along with the tendency of cables to follow along their own length when towed.

We recently added an algorithm to the data logger to estimate the peak to peak magnitude of the waveforms being recorded and to send these over a serial line to the serial data logger board. These data are telemetered to SUESI and the vessel, along with the pitch/roll/heading/depth data, every 10 s, in order to provide an indication of the status of the instrument and the size of the electric fields being recorded. We also added an acoustic altimeter to the transponder instrument on the far end of the array, and these data too are telemetered to the vessel via SUESI.

4.3. Time Correction Signal

Our data logger uses a Seascan Inc. time base, with specified drift rates of about 2 ms/d. We measure clock drift on recovery, but this does not indicate how linear the drift was over the period of deployment and temperature cycling between the surface and seafloor. At 33.5 Hz, the highest frequency used in the Gulf of Mexico project, a 2 ms time error translates to a 24° phase error, which is too large to include phase in inversions of data.

We address the limitations of the logger clocks by sending timing pulses from SUESI, whose waveform is controlled by GPS timing from the vessel, down the cable to the Vulcans. We added a device to SUESI which used the spare twisted pair of conductors in the tow cable to send a digital signal corresponding to the waveform transitions down to the Vulcans. This signal is then used to create an analog input to an unused channel on the data logger. We estimate that in this way time can be measured to better than 100 μ s,

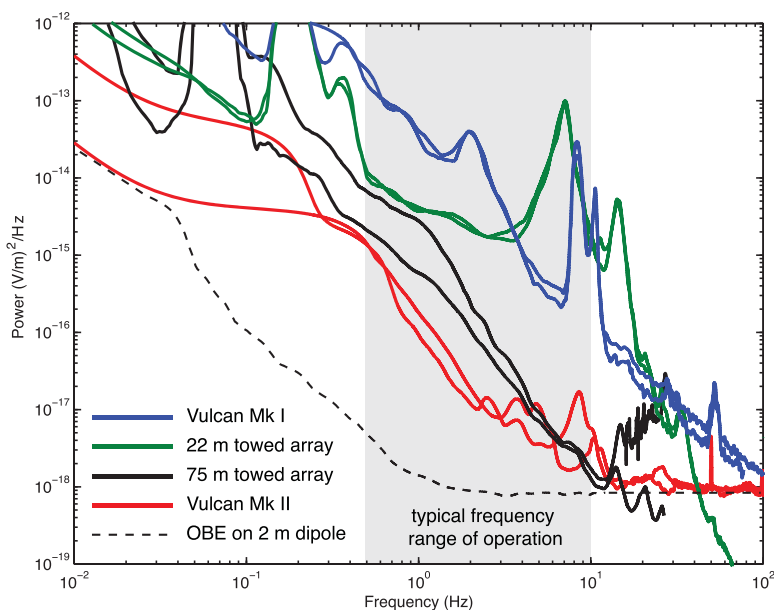


Figure 8. Electric field noise spectra of Vulcan instruments and cabled antennas towed through the water at speeds of 1.5–2 knots (0.75–1 m/s), which is typical of normal operations. The Vulcan Mk I data and 22 m cable data were collected during the Gulf of Mexico surveys described by *Weitemeyer and Constable*, [2010]. The 75 m cable data and Vulcan Mk II data were collected during midwater tests in the San Diego Trough, in 2006 and 2013, respectively. The broken black line shows the noise voltage on an OBE instrument normalized to a 2 m dipole.

allowing a phase accuracy of 1° at 33.5 Hz to be obtained. The timing data showed that the drift of the Seacan clocks is mostly linear, but that there is a timing offset in our data loggers of fraction of a sample, easily enough to compromise the accuracy of processed phase data.

5. Performance and Noise of the Vulcan System

Figure 8 shows electric field noise spectra from the 75 m antenna tests, along with noise spectra from a Mk-I instrument during the Gulf of Mexico survey described in *Weitemeyer and Constable*, [2010] which included a 22 m long cabled antenna attached to the tow cable in front of the Vulcan. Also shown are noise spectra from two Mk-II Vulcans towed on a 1 km array about 500 m deep in 1000 m water depth. These spectra show that there has been no compromise in making the instrument package smaller—indeed, noise performance is better in the Mk-II system, probably because flexing of the large fins and wings of the earlier system has been eliminated or at least reduced. These data were collected at towing speeds of 1.5–2 knots (0.75–1 m/s), which is typical of most CSEM deep-tow operations on account of the need to minimize layback given the large cross-sectional area of the deep-tow cable.

Strumming and vibration noise is evident between about 3 and 15 Hz, which is also seen in the accelerometer data. At frequencies above the strumming the noise floor is dominated by the amplifiers and is the same as that of a seafloor instrument. The noise peaks at around 5–10 s period are characteristic of vessel motion in the ocean swell being communicated along the towing cables, and is particularly strong in the Gulf of Mexico data.

Although towing a transmitter and receiver above the seafloor reduces receiver noise and allows rapid data acquisition in areas with rough seafloor or man-made obstacles, it does require that considerable effort be invested in constraining the geometry of the acquisition array. We can assess the effects on the data associated with errors in source-receiver geometry by carrying out a perturbation analysis using a simple 1-D model. We computed the sensitivity of typical horizontal electric field data to perturbations of position, attitude (pitch, roll, and yaw), and seawater electrical conductivity, as collected by a source and receiver system towed over a $1 \Omega\text{m}$ half-space at a height of 50 m in 1000 m water depth. The frequencies were 1.5, 3.5, and 6.5 Hz, the same as those used in the San Diego Trough test described below, but we modeled a

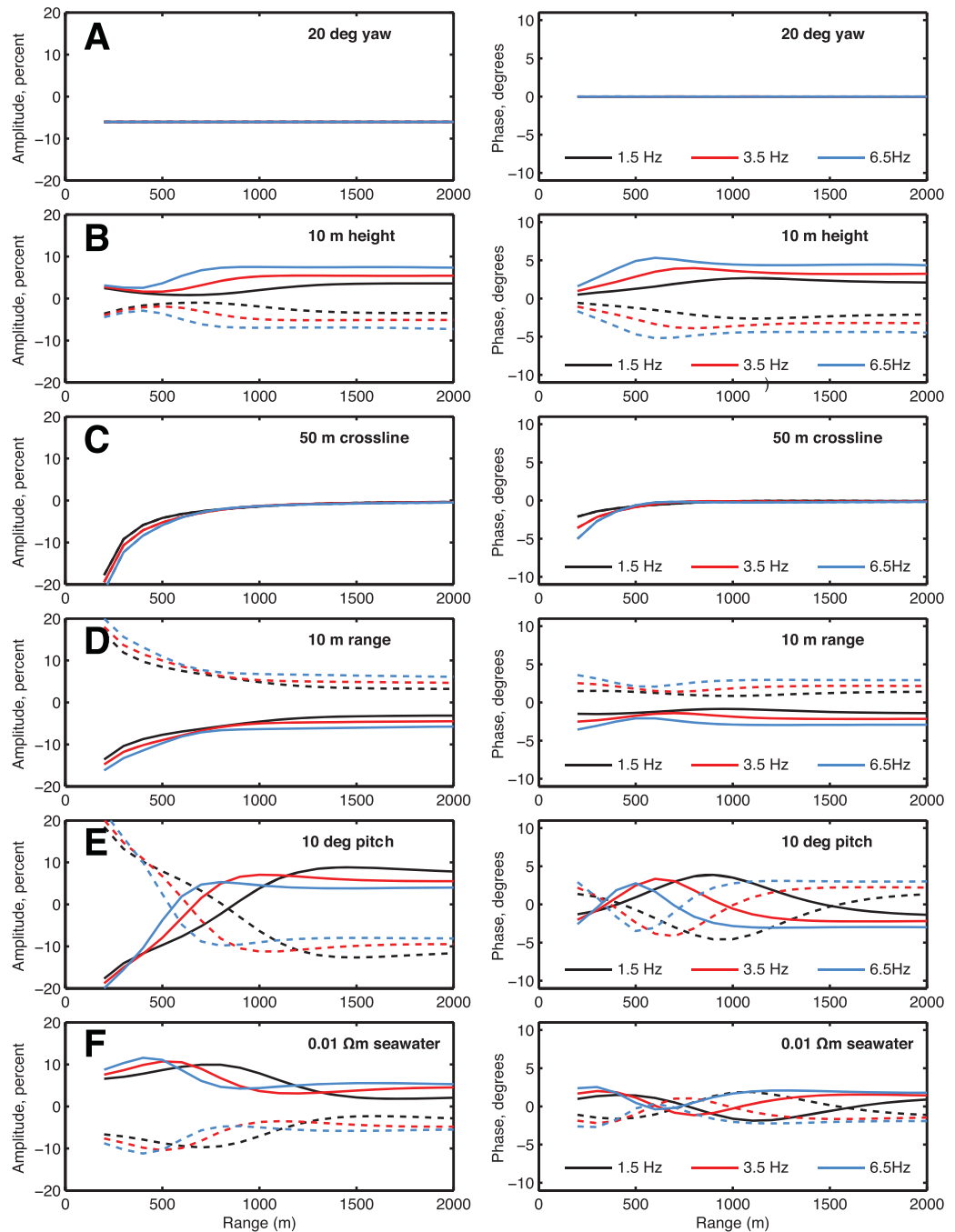


Figure 9. Error contributions for various navigation perturbations in horizontal electric field amplitude (left column) and phase (right column) as a function of source-receiver offset (range). The axes are scaled so that an amplitude of 100% equals a phase of one radian, and negative perturbations are plotted as broken lines. Calculations are for a 1 Ωm half space.

maximum range of 2000 m to represent the maximum source-receiver offset that might be realistically used this close to the seafloor.

The results of the perturbation analysis for the horizontal electric fields are presented in Figure 9. We have scaled the plots so that 10% in amplitude equals 5.7° in phase, which is the scaling that would apply to random errors in complex data [see, e.g., Myer *et al.*, 2011]. That is, a statistical processing error would have the same magnitude in both plots. The magnitudes of the perturbations are not based on realistic estimates, but have been chosen to be large enough to see the systematic effects in the data on one plot. Our phase

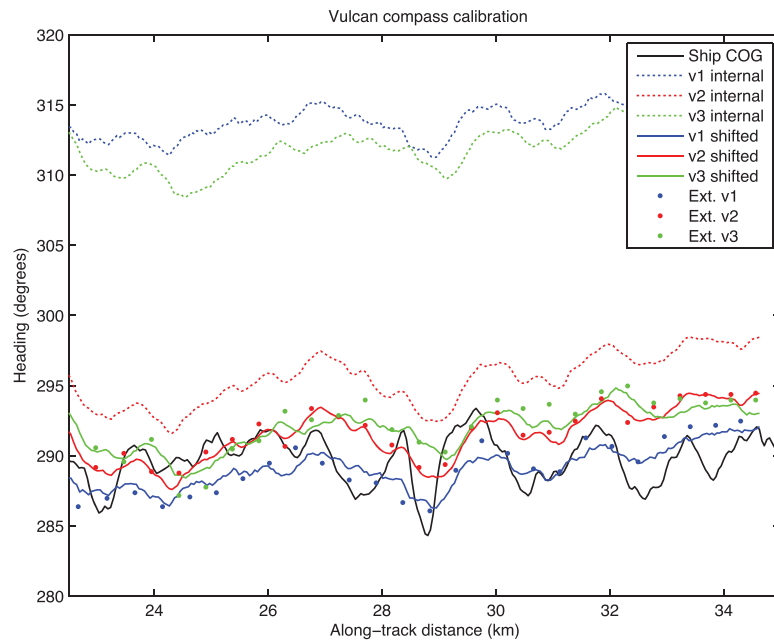


Figure 10. Data from the internal compasses during one tow, sampled every 2 s (broken lines) and data from external compasses sampled every 10 min (shown as dots). Solid lines show a single correction factor applied to each instrument to align the internal compass data with the external compass data. This correction is heading dependent, and so must be applied line by line. The black line is the ship's course over the ground. Vulcan 4 did not have an external compass and so is not shown.

convention is such that phase becomes increasingly negative with range, and we have assumed a point dipole transmitter. We have plotted positive perturbations as solid lines and negative perturbations as broken lines, because the effects are not linear, they are not always symmetrical, and the sign of the perturbation is not always the same in amplitude and phase.

Yaw (Figure 9a), or error in heading, is simplest to understand, since in a 1-D or 2-D model the crossline fields are zero. There is thus a simple range and frequency independent $\cos(\theta)$ decrease in amplitude with no effect on phase. The sign of the navigation error does not change the sign of the data error. That is, a clockwise rotation has the same effect as an anti-clockwise rotation.

Measurements of heading are made with magnetic compasses mounted inside the Vulcan instrument case and sampled at a relatively high rate of once every 2 s. However, these measurements are susceptible to magnetic fields generated by the instrument (especially batteries). In order to quantify this error, we mounted external compasses on the outside of the package near the electrodes. Because of size and power restrictions, these compasses sampled only every 10 min. However, we can show that for a given tow heading, a single additive correction factor can bring the internal compasses into agreement with the external compasses, allowing us to use the higher sample rate data for processing and modeling (Figure 10). We estimate that a realistic error on heading is about 2° .

Variations in receiver depth (Figure 9b), or distance from the seafloor (altitude), also produce relatively simple effects. Decreasing altitude increases both amplitude and phase, and increasing altitude does the opposite. At short ranges the effect is relatively small, since it is largely associated with the geometry of a dipole field in seawater, but at a range equal to about two skin depths in the seafloor (i.e., about 1000 m at 1.5 Hz and 500 m at 6.5 Hz) the effect increases and becomes constant with range, reflecting the change in number of skin depths in seawater between the seafloor and receiver. The effect increases with frequency because the skin depths get smaller.

Depth is measured to a fraction of a meter using pressure gauges and acoustic altimeters, and so an error of 1 m on depth would be considered conservative.

We consider a fixed crossline offset, independent of range, as shown in Figure 9c. If the array is set sideways at a constant angle by a cross-current, the offset from the nominal tow path would increase with range, but

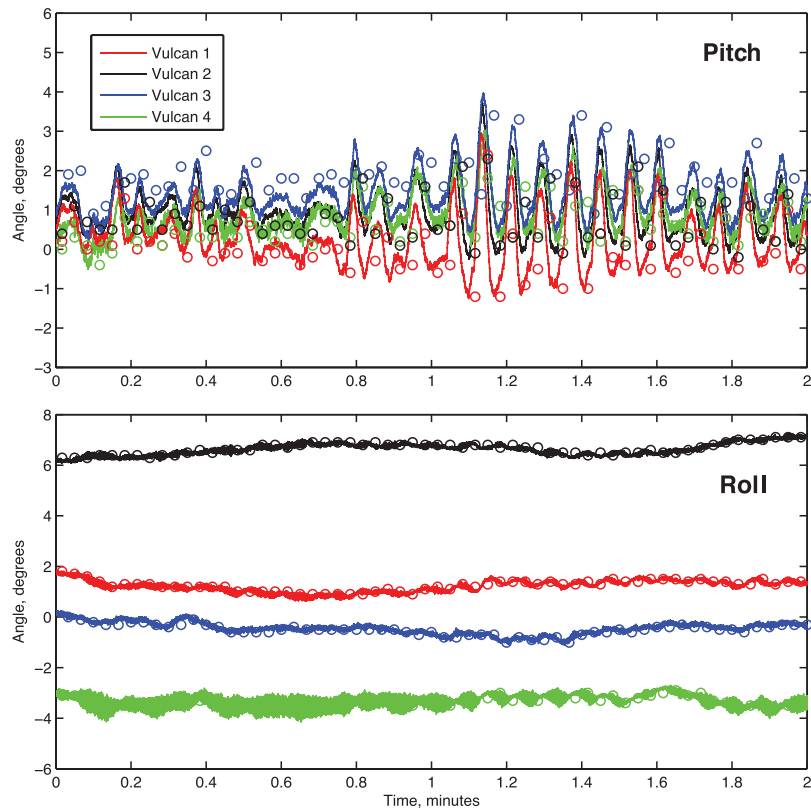


Figure 11. Two minutes of pitch and roll data collected on the internal compass/tiltmeter every 2 s (circles) compared with pitch and roll derived from the accelerometer sampled at 250 Hz (solid lines). A baseline shift has been applied to remove a zero-offset from the accelerometer data.

we would expect the transmitter antenna also to be at this angle and the inline geometry to be preserved. Errors would then not be processing or modeling errors, but rather an error in placing the resulting models in a geographical framework. The fixed offset we use here attempts to model bending of the array as it is towed through the water.

Crossline set has a much larger effect in amplitude than phase, and it decreases rapidly with range as it becomes proportionately smaller. It is not sensitive to sign, since the fields are symmetric across the tow line. The effect increases with frequency.

It is difficult to estimate crossline set without putting acoustic transponders on every Vulcan, and even then the errors in the acoustic locations are likely to be comparable to the signal we are trying to measure. Based on the behavior of the array on the sea surface, and examination of data, we would consider a 10 m error to be a conservative estimate.

Overestimating range (Figure 9d) decreases both amplitude and phase, and underestimating range does the opposite, which is as one would expect. The error on amplitude decreases with range because it becomes proportionately smaller, but the effect on phase is mostly constant with range because the rate of phase shift is proportional to the total number of skin depths between source and receiver. The effect is smaller on phase than on amplitude and increases with frequency.

Since the array consists of a cable which includes a para-aramid strength member, source-receiver range should be precisely set, to better than 1 m. However, if there is significant crossline set (as we have defined it above), then the effective length of the array will be proportionately reduced: a 5% crossline set will produce about a 0.2% decrease in range, amounting to 2 m in a 1000 m array. However, during a field test in which we acoustically ranged on the far end of a 1100 m array from the transmitter, we observed a standard deviation in the ranges of about 1 ms two way travel time, or 0.75 m. Since 1 ms is about what we estimate the error of the acoustic ranging system to be, this sets an upper bound on the amount of range variation.

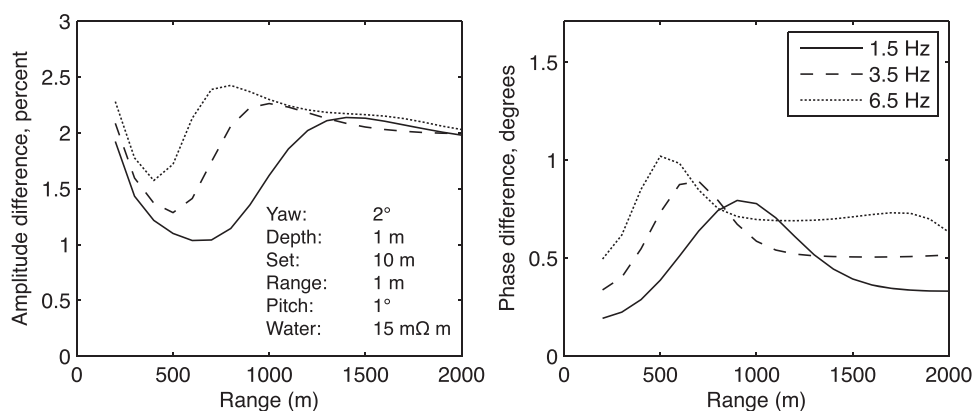


Figure 12. Geometric sums of the effect on horizontal electric field data of typical navigation errors given in the figure. Errors in transmitter yaw, depth, and pitch have been added to errors in receiver navigation. Calculations are for a 1 Ωm half space.

Roll does not contribute to errors in horizontal electric field measurements, and only has a $\cos(\theta)$ effect on vertical fields. The effect of pitch (Figure 9e) is somewhat complicated since it depends on the relative magnitude and phase of the vertical and horizontal fields. At a range equal to about one skin depth in the seafloor, the amplitude changes sign from a negative to a positive correlation with the sign of the navigation error, and then saturates at an almost frequency independent value. This is because the vertical field transitions from being small and out of phase with the horizontal field close to the transmitter to in-phase with a comparable amplitude as induction within the seafloor dominates. The phase error peaks near the point where amplitude becomes range-independent, and then becomes constant at long range.

Pitch and roll are logged from the compass/tiltmeter by the serial data logger in the main pressure case every 2 s, but are also captured by the accelerometer, which is sampled by the main data logger at (typically) 250 Hz. The x component acceleration couples directly into the roll of the instrument package and the y component acceleration couples into the pitch, and so we can directly compare accelerometer data to the compass pitch and roll (Figure 11). The agreement is excellent, and demonstrates that the scatter in the compass pitch is a result of the 5–10 s swell motion being passed down the cable. During CSEM processing, we take the mean values of pitch and roll over the 1 min stack frames, and Figure 11 shows that this will capture the average attitude of the instrument faithfully. We estimate that pitch is recorded to 1° accuracy or better. Note that we do not use pitch and roll to rotate the electric field data into horizontal and vertical components, but rather include them in the forward modeling to predict the fields as measured.

The effect of using an incorrect seawater conductivity in the modeling (Figure 9f) is significantly larger in amplitude than phase, and increases with frequency. A 3% (0.01 Ωm) increase in water resistivity increases amplitude between 1 and 5% and increases phase by 1° or less. We measure water conductivity continuously using a CTDV sensor with a stated accuracy of 0.001 S/m, and variations in seawater conductivity that are somewhat larger than this are observed along tow lines.

Because of reciprocity, the effects of errors in determining the transmitter geometry are the same as for the receivers, although only transmitter depth, pitch, and yaw contribute additional errors. All of the effects other than height and yaw depend on seafloor conductivity—decreasing seafloor conductivity decreases the effect of these other navigation errors. Every navigation error other than altitude has a proportionately larger effect on amplitude than phase, which was noted by *Myer et al.* [2012], who also observed this in repeat sampling of real data.

We can compute a geometric mean of our best estimates of the various navigation errors, adding independent depth, pitch, and yaw errors in the transmitter to the receiver errors (Figure 12). As expected, the effect on phase is smaller than amplitude, which suggests that if an error floor is being added to processing errors to account for uncertainties in navigation, one might not want to use the usual relationship that 100% in amplitude corresponds to 57.3° (one radian) in phase. The overall errors are smaller than for the deployed receiver case considered by *Myer et al.* [2012], and phase uncertainties of less than half a degree are probably smaller than errors in the calibration of the receivers and characterization of the transmitter waveform.

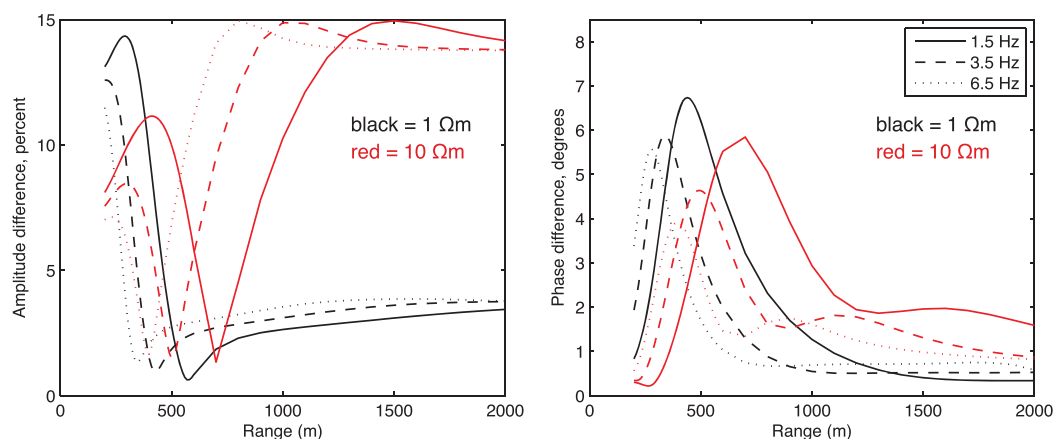


Figure 13. Geometric sums of the effect on vertical electric field data using similar parameters to Figure 12, but for two different seafloor resistivities (1 Ωm in black, 10 Ωm in red).

It should be noted that many of the navigation errors will not behave as random, independent errors. We can see from Figure 11 that pitch may act as a random error, as does depth, since both these parameters vary minute by minute. However, yaw, range, set, and water conductivity are likely to vary much more slowly, perhaps hour by hour, and so may behave more like systematic errors. Calibration errors in the receivers and navigation sensors will behave as truly systematic errors. Recognizing this, the error estimates presented in Figure 12 may underestimate how well we can fit the data in practice.

If we carry out a similar perturbation study on vertical electric field data, we discover that error is dominated by pitch, because tilting the instrument couples the larger horizontal fields into the vertical measurement. Data errors of 15 percent can be generated from pitch errors of only 1° (Figure 13). Furthermore, seafloor resistivity has a profound effect on the vertical electric field (which is why we measure it), and alters the predicted errors. Unlike the horizontal field, where effects of navigation error tend to increase with frequency, for the vertical field the error is largest at the lowest frequency.

6. 2015 San Diego Trough Tests

In March 2015, we carried out a deployment of the Vulcan-II system in the San Diego Trough, offshore southern California, to test the first implementation of the timing signal and the data waveform samples. Figure 14 shows the location of the tests, which started at a site in the southern part of the Trough where we had seafloor instruments deployed, and then targeted a known methane vent to the north. In their study of the San Diego Trough Fault, *Ryan et al.* [2012] carried out high-resolution bathymetry on a pop-up structure between two strands of the fault. They identified pock-marks and predicted venting of fluids or gas. In 2012 a group of graduate students from Scripps Institution of Oceanography followed up with bottom sampling and further geophysical studies, concluding that the venting was indeed methane [*Maloney et al.*, 2015]. In late 2012, we towed a Contros methane sensor over the vent and measured elevated methane concentrations, although unfortunately the methane sensor had not been properly calibrated by the manufacturer and so the results were not quantitatively useful.

For the March 2015 tests, we towed four Vulcan-II instruments at source-receiver offsets of 150, 250, 350, and 450 m, transmitting Waveform-D [*Myer et al.*, 2011] with a fundamental frequency of 0.5 Hz. Towing speed was about 1.5 knots and we used a 50 m source antenna with an output current of 100 A. In Figure 15, we show the navigational parameters for the 45 km long tow in 1000 m water depths from south to north along the San Diego Trough. At the north end of the line, we towed over the vent, made a turn, and towed over the vent a second time along a different heading. The transmitter tow height was 50 m, but because the array was trimmed slightly positively buoyant, the far end was flying 50 m above the transmitter, or about 5.7° from horizontal. The progression of flying heights is fairly uniform, so the array is fairly linear. In spite of the depth differences, the pitch of the Vulcan instruments is within about 1° of horizontal, with a scatter of $\pm 1^\circ$ due to the effects of sea swell on the tow cable. The A-TET on the end of the transmitter antenna is $5\text{--}7^\circ$ nose down,

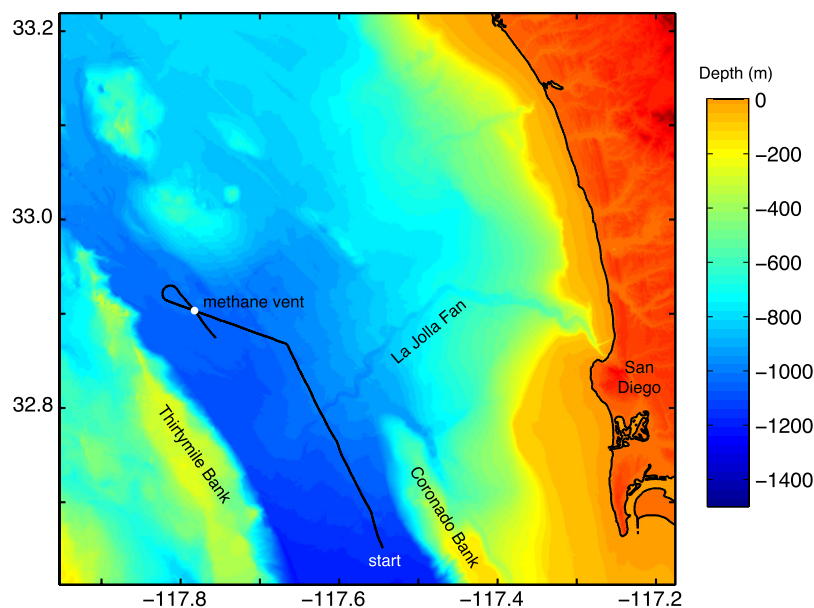


Figure 14. Map of the San Diego Trough showing the ship track of the tests carried out in 2015.

probably as a consequence of providing buoyancy for the copper transmission electrode. The pitch departs from horizontal by as much as 5° when towing over the small channel associated with the western end of the La Jolla Canyon as it cuts across the north side of the Coronado Bank.

Average roll is between $\pm 5^\circ$ depending on the instrument, with $\pm 3^\circ$ of short-period variability. The departure from zero for the average roll may be associated with imperfections in the split rope that we use to attach the Vulcan tow body, or it may be a result of lateral currents affecting the array. Because this project was initially intended only as an engineering test, we had not installed an acoustic navigation system to monitor the position of the array.

As part of our efforts to keep the power consumption low, the microprocessor chosen for the data logger is not computationally powerful enough to carry out real-time Fourier analysis of the electric fields. Instead, we implemented an algorithm to measure the amplitude of the transitions in the inline electric field data associated with the current switching in the transmitter. This rather crude measure, however, tracks variations in processed data very well. In Figure 16, we plot the real-time data samples, measured in ADC counts but here normalized to about 1, alongside 60 s stacks of 1.5 Hz data (the third harmonic of the 0.5 Hz fundamental) processed using the algorithm described in Myer *et al.* [2011], also normalized. The electric fields are about 15% larger directly over the methane vent, which was obvious on the vessel during the survey. Although we planned to carry out the turn over the vent site anyway, it is clear that the real-time estimates of field amplitudes would allow a survey to be modified to collect more data in areas of interest. The real-time data also confirms that the otherwise autonomous Vulcans are operating correctly.

We inverted inline and vertical amplitude and phase data from the three Vulcans at longest offsets, using frequencies 1.5, 3.5, and 6.5 Hz. We initially used an error floor based on our perturbation analysis. However, after some initial inversions, we concluded that the errors in the vertical field should be reduced by a quarter and the inline phase errors increased to about 1%. We found that it is difficult to fit the data from the Vulcan at 150 m offset because of the large effects of navigation errors at this short range, and so this instrument was excluded from the inversion. We used the 2-D inversion code of Key [Key and Ovall, 2011; Key, 2012] which is based on the Occam inversion algorithm [Constable *et al.*, 1987]. Although this code exploits a triangular unstructured finite element mesh for the forward calculations, the inversion was carried out on a quadrilateral parameter mesh that conforms to bathymetry. This stabilizes the inversion and

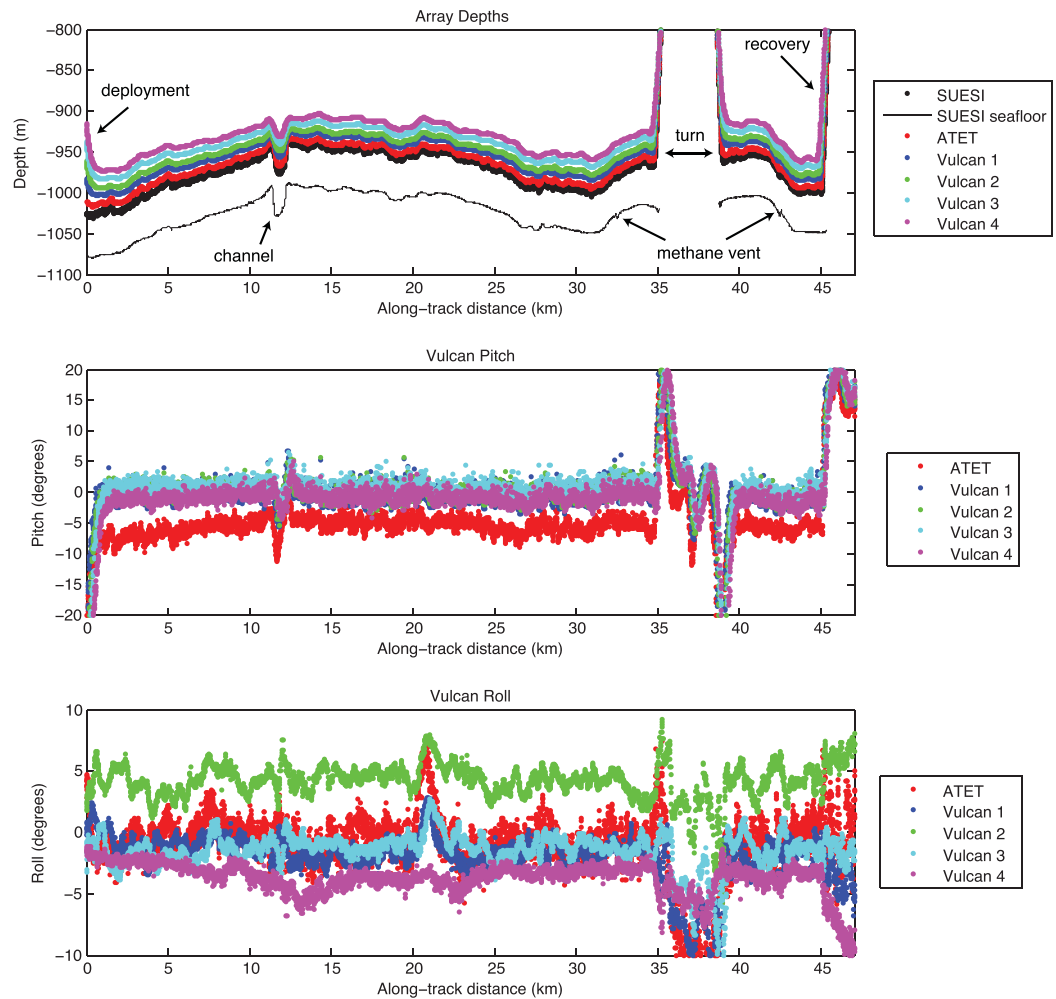


Figure 15. Navigation data from the array components during a test in 1000 m water in the San Diego Trough.

reduces the number of parameters when the lateral dimension of the model is much larger than the vertical dimension, as it is here. Conductivity was allowed to vary between the vertical direction and the horizontal directions (transverse isotropy around the vertical direction, or polar anisotropy). The length of the 50 m transmitter antenna is significant at the short Vulcan offsets, so we integrated point dipole fields along the actual antenna length in the modeling.

In Figure 17, we show the vertical resistivity of the line between the turn near the middle of the tow and the first crossing of the methane vent. The inversion was started from a $1 \Omega\text{m}$ half-space and converged to an RMS misfit of 1.0 in six iterations. The seafloor structure is bland, with an increase in resistivity from about $1 \Omega\text{m}$ to about $3 \Omega\text{m}$ at around 200 m depth, with the exception of a resistor under the vent site. We show more detailed inversions of the vent site below, but present this figure to show that the vent site is unusual, that there are few artifacts in the inversion model, and that our error model seems to work. As is usual for marine sediments, the horizontal resistivities are somewhat lower than the vertical resistivity shown here, but the general structure is the same.

Figure 18 shows the 1.5 Hz data along with inverted responses of the model shown in Figure 17 for Vulcan 4, at the largest source-receiver offset. The peak in amplitude and phase at -5.5 km is the response of the resistive methane seep, but the 100 m scale fluctuations are associated with navigational variations in the system, mostly depth and pitch. The model response and data track extremely well, to a fraction of a percent and a fraction of a degree in E_y . The processing and navigation errors for the E_z data are larger, but the signal from the vent structure is also larger in the vertical field.

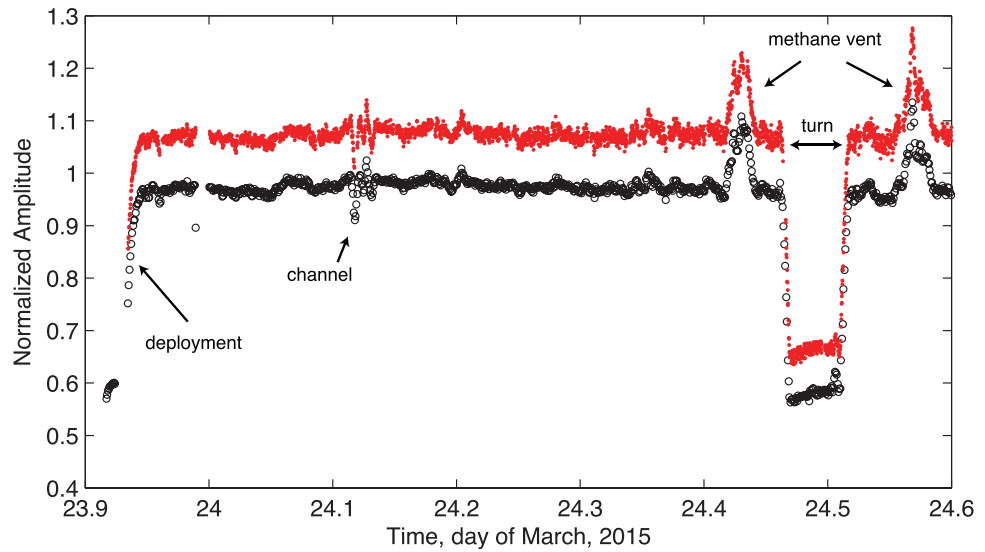


Figure 16. Comparison between real-time sampling of waveform amplitudes (red dots) and 60 s stacks of processed CSEM data at 1.5 Hz (black circles) on the 500 m Vulcan. The two passes over the methane vent are evident at day 24.425 and day 24.575. The small data gap just before midnight on the 24th is a result of the transmitter being switched off.

There is a systematic bias in some of the fits, which is also the case for some of the 32 other data components not shown. The bias is roughly evenly distributed between positive and negative residuals. *Gehrmann et al. [2015]* include a “calibration factor” in the inversion to remove such bias, but our approach is to constrain the experimental parameters sufficiently well that this is not necessary. Since the bias is within the error bars, which for the inline component are about 1% in amplitude and 1° in phase, we do not consider it a serious problem. At least some of the bias is associated with the regularization in the smooth inversion, which can be seen in the inline phase, which is choosing to underfit the signal from the methane vent.

Prior to this test, we had difficulty inverting phase data from the Vulcan instruments, but here we were able to use the timing signal sent down the tow cable to correct for clock errors during the survey. Figure 19 shows an example of three transmitter waveforms digitized on Vulcan number 4 at three different times during the tow. The timing pulses are coming in 19–21 ms late and represent a clock error of this magnitude. A 20 ms error in clock drift is about a 40° phase error at the highest frequency inverted, but using the timing information allows this to be corrected.

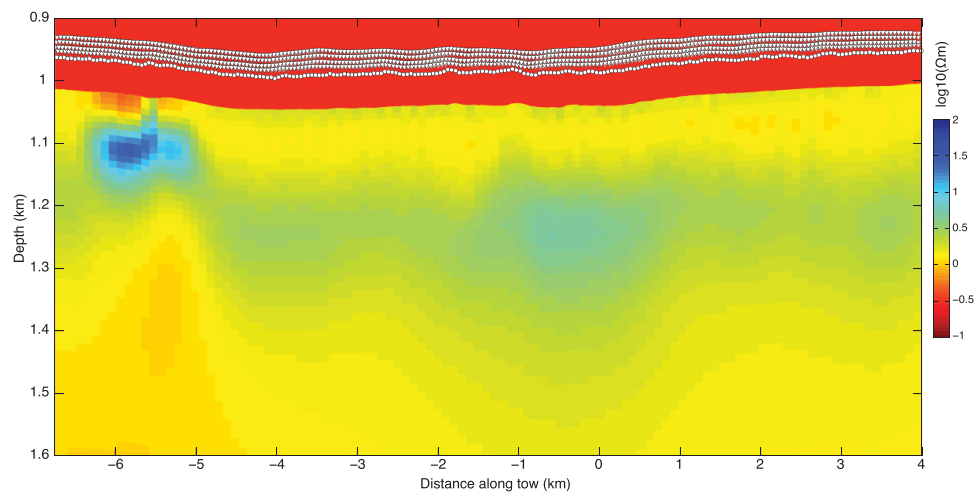


Figure 17. Inversion of inline and vertical amplitude and phase data from Vulcans 2, 3, and 4 between the mid-trough turn and the first crossing of the methane vent. The data are fit to RMS 1.30 with a noise floor based in the perturbation analysis shown in Figures 12 and 13.

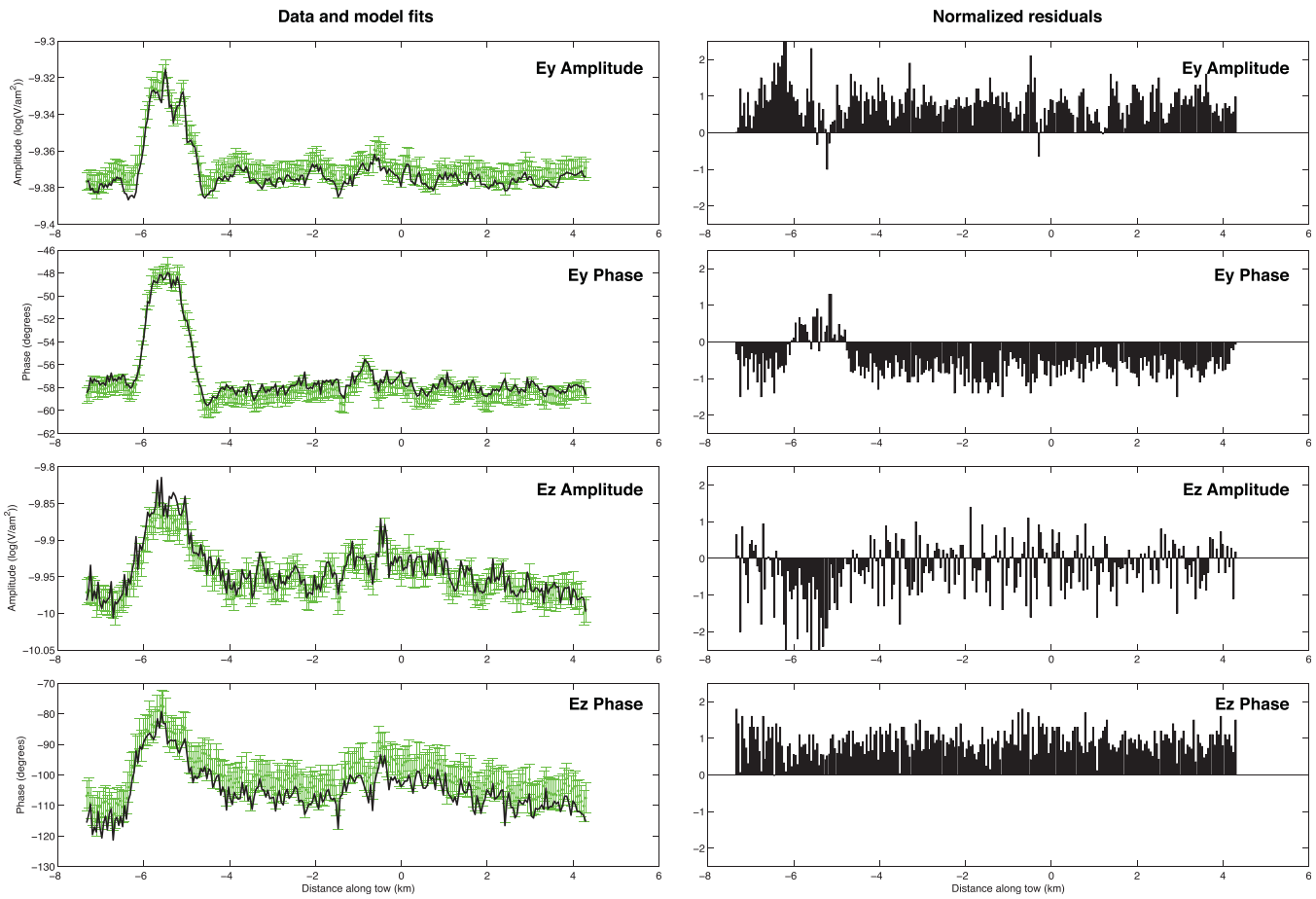


Figure 18. Data (symbols with one sigma error bars), model responses (solid black lines), and normalized residuals for one frequency (1.5 Hz) and one instrument (Vulcan 4) for the inversion shown in Figure 17. Note that the axes are individually scaled, and that this represents only one ninth of the entire data set inverted. The high spatial frequency signal is primarily associated with variations in navigation geometry, such as pitch, heading, and altitude, and is well tracked by the model, but systematic bias remains. The peak in amplitude and phase at -5.5 km is the response of the methane seep.

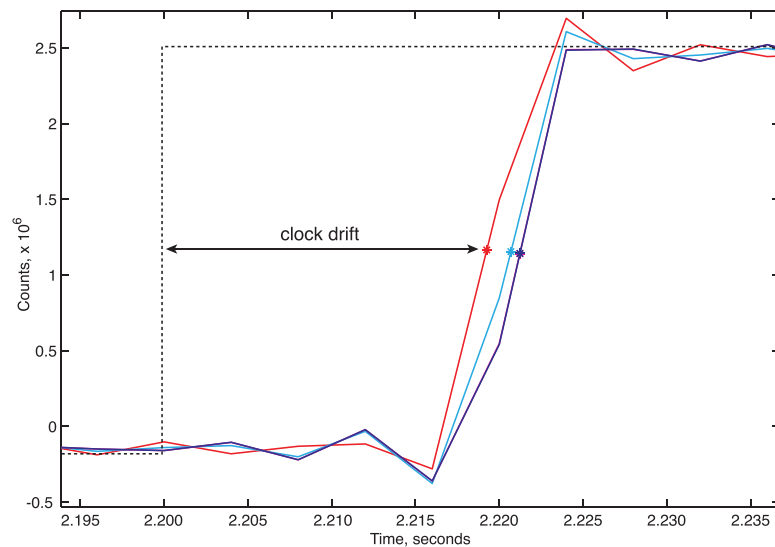


Figure 19. Timing pulses digitized on Vulcan 4 at three times during the tow. The waveform transition should have arrived at 2.200 s (illustrated by the broken black line). Instead they are being digitized 19–21 ms late. The data points are a timing pick at half the height of the transition.

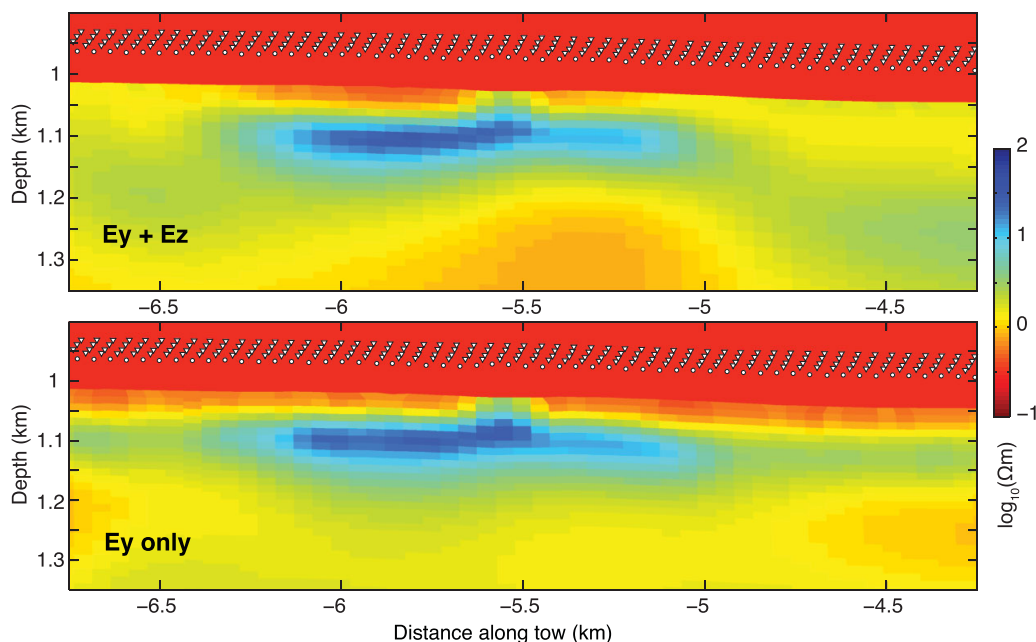


Figure 20. Vertical resistivity from inversions of Vulcan data during the first crossing of the methane vent. (top) Both inline and vertical electric fields, while the (bottom) is an inversion of the inline fields only. The sense of the distance along tow is positive toward the southeast.

Figure 20 shows inversions of the vent area for the first crossing using a finer discretization for the parameter mesh than for the inversion of the entire line (inversion of the second crossing is almost identical). We have inverted inline data only, which fits to about RMS 1.0, and both inline and vertical data, which fits to about RMS 1.6. The larger misfit for the vertical field may be because our error model, based on a 1 Ωm seafloor, breaks down over the vent. Both inversions contain a resistive feature beneath the known location of the methane vent. The inclusion of the vertical field data appears to constrain the uppermost seafloor resistivity, which is what one would expect from the galvanic sensitivity of this component, and has removed what appears to be spurious layering to the sides of the model. A conductor has appeared beneath the vent, which may be associated with the faulting that is thought to be bringing methane from depth.

The resistive feature starts about 50 m below seafloor and extends to about 150 mbsf, which means the feature is almost certainly within the gas hydrate stability field, and so is likely hydrate rather than free gas. However, we see a “conduit” to the surface about 100 m wide and coincident with the pockmarks observed by Ryan *et al.* [2012] and the methane venting, acoustic wipeout, and chemosynthetic biota observed by Maloney *et al.* [2015] and Grube *et al.* [2015]. Maloney *et al.* [2015] observe offsets in sediment horizons imaged by acoustic data on either side of the wipeout zone, suggesting that it is associated with a fault. Likely, then, we have imaged methane migration along a fault (or faults) associated with the San Diego Trough Fault system, along with gas hydrate forming within its stability field along the sides of the fault. The resistivities of 30 Ωm are significantly higher than have been previously observed in marine EM hydrate studies [Goto *et al.*, 2008; Weitemeyer *et al.*, 2010; Schwalenberg *et al.*, 2010a,b; Goswami *et al.*, 2015; Gehrman *et al.*, 2015]. Hydrate and sediment mixtures without free water have a resistivity of about 2000 Ωm [Du Frane *et al.*, 2015], so a simple Archie’s Law calculation using this matrix resistivity, a pore space filled with seawater, and a porosity exponent of 2 suggests a liquid water content of only about 10%. Although there are as yet no laboratory conductivity data on methane hydrate/sediment mixes containing sea water, and the use of Archie’s Law is subject to errors [e.g., Lee and Collett, 2001], the conclusion is that these high resistivities suggest high levels of hydrate saturation.

7. Discussion

Our towed receiver system was originally designed to be used in conjunction with deployed seafloor electromagnetic receivers, in order to help constrain near-seafloor conductivity structure between instruments.

However, by adding multiple receivers on the towed array and processing a broad range of frequencies, the Vulcan system can act as a stand-alone method to investigate geology in the uppermost seafloor when deeper structure is not of interest. For example, in the summers of 2014 and 2015, the system was used by the Japanese National Institute of Advanced Industrial Science and Technology (AIST) to collect 1000 km of Vulcan-only data over a gas hydrate prospects in 400–1100 m water.

Besides avoiding the ship time required to deploy and recover seafloor instruments, another advantage of a survey using only towed instruments is that it places much less demand on the navigation system. Myer *et al.* [2012] showed that an error of only 5 m in source-receiver range amounted to 1–2% error in CSEM amplitudes at ranges below 2 km for 0.25 Hz OBEM data. Depending on the type of acoustic navigation system used, errors could amount to ten times this, and for higher frequencies the errors will also be greater. However, the towed receiver system is largely immune to inline source-receiver range errors. Transmitter navigation is only required to place inverted models on a map—in the San Diego Trough test the transmitter was navigated simply by using ship's position and layback, yet the data could be fit to 1% in the inversions. Note that accurate transmitter navigation is not required in order to include bathymetry in the inversions, since the transmitter measures both its depth and altitude. In fact, bathymetry obtained this way can also be used to align the data with existing maps.

It is likely that the denser sampling, better navigational control, and low noise associated with the Vulcan towed system results in much better resolution of seafloor structure than can be obtained using only seafloor receivers. There is the suggestion that depth sensitivity may be comparable to maximum source-receiver separation, which is better than one would expect for seafloor instruments. The inversions presented above have features extending 500 m below the seafloor, and inversions of data collected with a 1000 m array have resistivity structures coincident with seismic structures at depths of 1000 m [Constable and Kannberg, 2015].

8. Conclusions

We have developed a continuously towed, three-axis, CSEM electric field receiver. By careful control of buoyancy, along with real-time information on array depth, we have been able to tow 1200 m long arrays of instruments within 50–100 m of the seafloor. High-frequency noise levels are comparable to deployed seafloor receivers if the shorter dipole lengths are taken into account. The instruments may be used as a stand-alone system for imaging seafloor to depths approaching the largest source-receiver separation and are well-suited to studies of seafloor gas hydrate, hydrothermal systems, or mineralization. The system can also be used to better control shallow structure in CSEM surveys for deeper targets using deployed receivers.

Acknowledgments

Engineering support provided by Jacques Lemire and John Souders of the Scripps Marine EM Laboratory was critical to the development of the Vulcan instrument system. We are extremely grateful to have access to the 2-D inversion code of Kerry Key, along with his help and advice. The Scripps Seafloor Electromagnetic Methods Consortium (<http://marineemlab.ucsd.edu/semc.html>) and the US Department of Energy (contract DE-NT0005668) provided support for the development of the Vulcan Mk-I system, while Fugro and Seabed Geosolutions supported the development of the Mk-II system. Particular thanks go to Kelly Callaway and Johannes Singer of Fugro for their encouragement and suggestions. Ocean Floor Geophysics funded the ship time for the 2015 tests and supported the AIST data collection. Support for P.K. was provided in part by U.S. Department of Energy contract DE-FE0010144. Digital versions of data used in this paper are available at <http://marineemlab.ucsd.edu>. We thank Romina Gehrmann, an anonymous reviewer, and the editors for suggestions to improve the manuscript.

References

- Cheesman, S.J., L.K. Law, and B. St.Louis (1993), A porosity mapping survey in Hecate Strait using a seafloor electro-magnetic profiling system, *Mar. Geol.*, *110*, 245–256.
- Constable, S. (2010), Ten years of marine CSEM for hydrocarbon exploration, *Geophysics*, *75*, 75A67–75A81.
- Constable, S. (2013), Review paper: Instrumentation for marine magnetotelluric and controlled source electromagnetic sounding, *Geophys. Prospect.*, *61*, 505–532.
- Constable, S., and C.S. Cox (1996), Marine controlled source electromagnetic sounding 2. The PEGASUS experiment, *J. Geophys. Res.*, *101*, 5519–5530.
- Constable, S., and P. Kannberg (2015), Marine electromagnetic survey of Santa Cruz basin, final report, Scripps Institution of Oceanography, La Jolla, Calif. [Available at <http://marineemlab.ucsd.edu/Projects/SantaCruz/>, accessed 15 Feb. 2016.]
- Constable, S. C., R. L. Parker, and C. G. Constable (1987), Occam's Inversion: A practical algorithm for generating smooth models from EM sounding data, *Geophysics*, *52*, 289–300.
- Constable, S., A. Orange, G. M. Hoversten, and H. F. Morrison (1998), Marine magnetotellurics for petroleum exploration Part 1. A seafloor instrument system, *Geophysics*, *63*, 816–825.
- Constable, S., P. Kannberg, K. Callaway, and D. Ramirez Mejia (2012), Mapping shallow geological structure with towed marine CSEM receivers, in *SEG Technical Program Expanded Abstracts*, pp. 1–5, Society of Exploration Geophysicists, Tulsa, Okla.
- Cook, A.E., D. Goldberg, and R.L. Kleinberg (2008), Fracture-controlled gas hydrate systems in the northern Gulf of Mexico, *Mar. Pet. Geol.*, *25*, 932–941.
- Cox, C.S. (1981), On the electrical conductivity of the oceanic lithosphere, *Phys. Earth Planet. Int.*, *25*, 196–201.
- Du Frane, W., L.A. Stern, S. Constable, K.A. Weitemeyer, M.M. Smith, and J.J. Roberts (2015), Electrical properties of methane hydrate + sediment mixtures, *J. Geophys. Res. Solid Earth*, *120*, 4773–4787, doi:10.1002/2015JB011940.
- Ellingsrud, S., T. Eidesmo, S. Johansen, M. C. Sinha, L. M. MacGregor, and S. Constable (2002), Remote sensing of hydrocarbon layers by seabed logging (SBL): Results from a cruise offshore Angola, *Lead. Edge*, *21*, 972–982.
- Evans, R. L. (2007), Using CSEM techniques to map the shallow section of seafloor: From the coastline to the edges of the continental slope, *Geophysics*, *72*, WA105–WA116.

- Gehrmann, R. A. S., J. Dettmer, K. Schwalenberg, M. Engels, S. E. Dosso, and A. Özmaral (2015), Trans-dimensional Bayesian inversion of controlled-source electromagnetic data in the German North Sea, *Geophys. Prospect.*, *63*, 1314–1333.
- Goldman, M., E. Levi, B. Tezkan, and P. Yogeshwar (2011), The 2D coastal effect on marine time domain electromagnetic measurements using broadside dBz/dt of an electrical transmitter dipole, *Geophysics*, *76*, F101–F109.
- Goswami, B. K., K. A. Weitemeyer, T. A. Minshull, M. C. Sinha, G. K. Westbrook, A. Chabert, T. J. Henstock, and S. Ker (2015), A joint electromagnetic and seismic study of an active pockmark within the hydrate stability field at the Vestnesa Ridge, West Svalbard margin, *J. Geophys. Res. Solid Earth*, *120*, 6797–6822, doi:10.1002/2015JB012344.
- Goto, T., et al. (2008), A marine deep-towed DC resistivity survey in a methane hydrate area, Japan Sea, *Explor. Geophys.*, *39*, 52–59.
- Grupe, B. M., M. L. Krach, A. L. Pasulka, J. M. Maloney, L. A. Levin, and C. A. Frieder (2015), Methane seep ecosystem functions and services from a recently discovered southern California seep, *Mar. Ecol.*, *36*, 91–108.
- Key, K. (2012), Marine EM inversion using unstructured grids: A 2D parallel adaptive finite element algorithm, in *SEG Technical Program Expanded Abstracts*, pp. 1–5, Society of Exploration Geophysicists, Tulsa, Okla.
- Key, K., and J. Ovall (2011), A parallel goal-oriented adaptive finite element method for 2.5-D electromagnetic modelling, *Geophys. J. Int.*, *186*, 137–154.
- Key, K., S. Constable, T. Matsuno, R. L. Evans, and D. Myer (2012), Electromagnetic detection of plate hydration due to bending faults at the Middle America Trench, *Earth Planet. Sci. Lett.*, *351–352*, 45–53, doi:10.1016/j.epsl.2012.07.020.
- Lee, M. W., and T. S. Collett (2001), Gas hydrate estimation error associated with uncertainties of measurement parameters, *U.S. Geol. Surv. Bull.*, *2182*, 8 p. [Available at <http://pubs.usgs.gov/bul/b2182/>, accessed 15 Feb. 2016.]
- MacGregor, L., M. Sinha, and S. Constable (2001), Electrical resistivity structure of the Valu Fa Ridge, Lau Basin, from marine controlled-source electromagnetic sounding, *Geophys. J. Int.*, *146*, 217–236.
- Maloney, J. M., B. M. Grupe, A. L. Pasulka, K. S. Dawson, D. H. Case, C. A. Frieder, L. A. Levin, and N. W. Driscoll (2015), Transpressional segment boundaries in strike-slip fault systems offshore southern California: Implications for fluid expulsion and cold seep habitats, *Geophys. Res. Lett.*, *42*, 4080–4088, doi:10.1002/2015GL063778.
- Müller, H., T. von Dobeneck, W. Nehmiz, and K. Hamer (2011), Near-surface electromagnetic, rock magnetic, and geochemical fingerprinting of submarine freshwater seepage at Eckernförde Bay (SW Baltic Sea), *Geo Mar. Lett.*, *31*, 123–140.
- Müller, H., T. von Dobeneck, C. Hilgenfeldt, B. SanFilipo, D. Rey, and B. Rubio (2012), Mapping the magnetic susceptibility and electric conductivity of marine surficial sediments by benthic EM profiling, *Geophysics*, *77*, E43–E56.
- Myer, D., S. Constable, and K. Key (2011), Broad-band waveforms and robust processing for marine CSEM surveys, *Geophys. J. Int.*, *184*, 689–698.
- Myer, D., S. Constable, K. Key, M. E. Glinsky, and G. Liu (2012), Marine CSEM of the Scarborough gas field, Part 1: Experimental design and data uncertainty, *Geophysics*, *77*, E281–E299, doi:10.1190/GEO2011-0380.1.
- Riedel, M., T. S. Collett, P. Kumar, A. V. Sathe, and A. Cook (2010), Seismic imaging of a fractured gas hydrate system in the Krishna-Godavari Basin offshore India, *Mar. Pet. Geol.*, *27*, 1476–1493.
- Ryan, H. F., J. E. Conrad, C. K. Paull, and M. McGann (2012), Slip rate on the San Diego Trough fault zone, inner California borderland, and the 1986 Oceanside earthquake swarm revisited, *Bull. Seismol. Soc. Am.*, *102*, 2300–2312, doi:10.1785/0120110317.
- Schwalenberg, K., and M. Engels (2011), Marine controlled source electromagnetic methods for gas hydrate assessment: New instrumentation and first field applications, in *Proceedings of the 7th International Conference on Gas Hydrates*, pp. 17–21, Edinburgh, U. K. [Available at <http://www.pet.hw.ac.uk/icgh7/papers/icgh2011Final00446.pdf>.]
- Schwalenberg, K., M. Haeckel, J. Poort, and M. Jegen (2010a), Evaluation of gas hydrate deposits in an active seep area using marine controlled source electromagnetics: Results from Opouawe Bank, Hikurangi Margin, New Zealand, *Mar. Geol.*, *272*, 89–98.
- Schwalenberg, K., W. Wood, I. Pecher, L. Hamdan, S. Henrys, M. Jegen, and R. Coffin (2010b), Preliminary interpretation of electromagnetic, heat flow, seismic, and geochemical data for gas hydrate distribution across the Porangahau Ridge, New Zealand, *Mar. Geol.*, *272*, 79–88.
- Sinha, M. C., P. D. Patel, M. J. Unsworth, T. R. E. Owen, and M. R. J. MacCormack (1990), An active source EM sounding system for marine use, *Mar. Geophys. Res.*, *12*, 59–68.
- Webb, S. C., S. C. Constable, C. S. Cox, and T. K. Deaton (1985), A sea-floor electric field instrument, *Geomagnet. Geoelect.*, *37*, 1115–1129.
- Weitemeyer, K., and S. Constable (2010), Mapping shallow geology and gas hydrate with marine CSEM surveys, *First Break*, *28*, 97–102.
- Weitemeyer, K., G. Gao, S. Constable, and D. Alumbaugh (2010), The practical application of 2D inversion to marine controlled-source electromagnetic sounding, *Geophysics*, *75*, F199–F211.
- Weitemeyer, K. A., S. C. Constable, K. W. Key, and J. P. Behrens (2006), First results from a marine controlled-source electromagnetic survey to detect gas hydrates offshore Oregon, *Geophys. Res. Lett.*, *33*, L03304, doi:10.1029/2005GL024896.
- Yuan, J., and R. N. Edwards (2000), The assessment of marine gas hydrates through electrical remote sounding: Hydrate without a BSR?, *Geophys. Res. Lett.*, *27*, 2397–2400.